The Astrophysical Journal, 575:1151–1162, 2002 August 20
© 2002. The American Astronomical Society. All rights reserved. Printed in U.S.A.

MAGNETOROTATIONAL INSTABILITY IN LIQUID METAL COUETTE FLOW

K. Noguchi
Los Alamos National Laboratory, T-CNLS, Los Alamos, NM 87545

V. I. Pariev[1,2] and S. A. Colgate
Los Alamos National Laboratory, T-6, Los Alamos, NM 87545

H. F. Beckley
Department of Physics, New Mexico Institute of Mining and Technology, Socorro, NM 87801

and

J. Nordhaus
Department of Physics and Astronomy, University of Rochester, Rochester, NY 14627
Received 2001 December 14; accepted 2002 April 30

ABSTRACT

Despite the importance of the magnetorotational instability (MRI) as a fundamental mechanism for angular momentum transport in magnetized accretion disks, it has yet to be demonstrated in the laboratory. A liquid sodium $\alpha\omega$ dynamo experiment at the New Mexico Institute of Mining and Technology provides an ideal environment to study the MRI in a rotating metal annulus (Couette flow). A local stability analysis is performed as a function of shear, magnetic field strength, magnetic Reynolds number, and turbulent Prandtl number. The latter takes into account the minimum turbulence induced by the formation of an Ekman layer against the rigidly rotating end walls of a cylindrical vessel. Stability conditions are presented, and unstable conditions for the sodium experiment are compared with another proposed MRI experiment with liquid gallium. Because of the relatively large magnetic Reynolds number achievable in the sodium experiment, it should be possible to observe the excitation of the MRI for a wide range of wavenumbers and to further observe the transition to the turbulent state.

Subject headings: accretion, accretion disks — instabilities — MHD — plasmas

1. INTRODUCTION

A significant problem in accretion disk theory is the nature of anomalous viscosity. In order for accretion to occur, angular momentum must be transported outward. The central problem in astrophysical accretion disks is that observed accretion rates cannot be due to ordinary molecular viscosity. A robust anomalous angular momentum transport mechanism must operate in accretion disks.

In 1991, the magnetorotational instability (MRI), discovered by Velikhov (1959) and Chandrasekhar (1960), was reintroduced as a mechanism for excitation and sustaining MHD turbulence in a magnetized but Rayleigh-stable fluid by Balbus & Hawley (1991). Since then, many numerical and analytic studies of the MRI have been performed under varying conditions (Hawley & Balbus 1991; Matsumoto & Tajima 1995; Hawley, Gammie, & Balbus 1996; Stone et al. 1996; Gammie 1996; Sano & Miyama 1999; Noguchi, Tajima, & Matsumoto 2000; Sano & Inutsuka 2001). Nevertheless, amidst all the theoretical attention granted to the MRI, it has never been demonstrated in the laboratory. In light of this fact, an $\alpha\omega$ dynamo experiment at the New Mexico Institute of Mining and Technology provides a unique opportunity to study the MRI in a rotating metal annulus using liquid sodium. In this paper, a local stability analysis is performed, and the results are compared with theoretical analysis from a similar proposed experiment at the Princeton Plasma Physics Laboratory (PPPL; Ji, Goodman, & Kageyama 2001; Goodman & Ji 2001). Varying aspects of the experiments are discussed, with stable and unstable regions identified in terms of magnetic field strength and shear flow. In addition, the number of unstable modes and the Prandtl number further define the parameter space. If the number of unstable modes is large compared to unity, then there exists the possibility of observing turbulence generated by the MRI. Finally, we investigate the instability boundary when fluid turbulence is injected as, for example, through the Ekman layer flow.

2. NEW MEXICO $\alpha\omega$ DYNAMO EXPERIMENT

The New Mexico $\alpha\omega$ dynamo (NMD) experiment is a collaboration between the New Mexico Institute of Mining and Technology and Los Alamos National Laboratory (Colgate et al. 2001). The experiment is designed to create an astrophysical dynamo, the $\alpha\omega$-dynamo, in a rapidly rotating laboratory system. The apparatus consists of two coaxial cylinders (Fig. 1), rotating at different angular velocities and therefore creating Couette flow in the annular volume. Liquid sodium fills the volume between the cylinders and the end walls. Solid plates attached to and corotating with the outer cylinder with an angular velocity, Ω_2, define the end walls. (In addition, for the dynamo experiment, an external source of helicity is supplied, driven plumes, but this is not part of the MRI experiment.) The schematic of the flow field (Fig. 1) places particular emphasis on the primary diagnostic of multiple, three-axis, magnetic field Hall effect detectors (sensitivity: 0.1–10 kG), located in aerodynamically shaped probes within the rotat-

[1] Lebedev Physical Institute, Leninsky Prospect 53, Moscow 117924, Russia.

[2] Currently at Department of Physics and Astronomy, University of Rochester, Rochester, NY 14627.

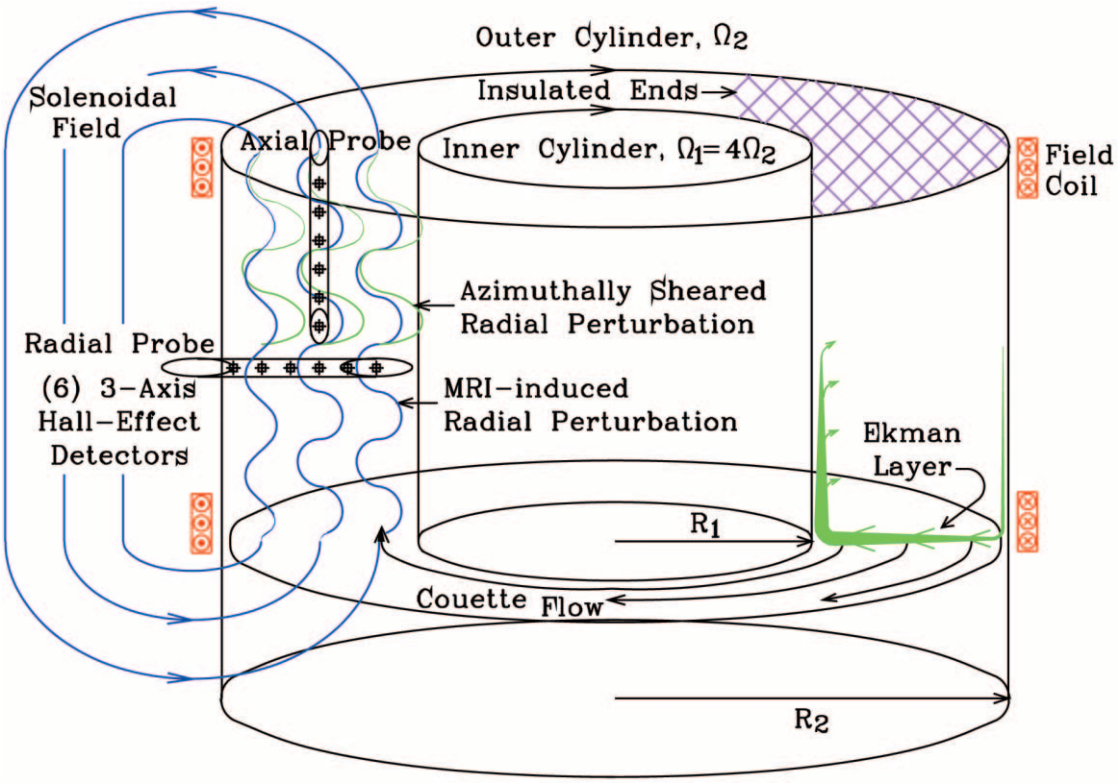


FIG. 1.—Schematic drawing of the New Mexico Institute of Mining and Technology Ω-phase of the $\alpha\omega$ dynamo experiment. The inner cylinder is rotated relative to the outer or main cylinder of radius $R_2 = 30.5$ cm at Ω_2, and where the inner cylinder of $R_1 = 15.2$ cm is rotated at Ω_1. The ratio Ω_1/Ω_2 can be adjusted from unity to infinity by a brake on Ω_2, not shown, and where Ω_1 is driven. A fixed gear ratio also allows the maximum shear case at marginal stability, $\Omega_1/\Omega_2 = (R_2/R_1)^2 = 4$, to be obtained. An axial or quadrupole magnetic field is supplied by coils, also shown schematically. The magnetic field internal to the liquid sodium in the annular space between the two cylinders and bounded by the end walls (corotating with the outer cylinder) is measured by an aerodynamically shaped probe containing six three-axis Hall detectors. These detectors can measure fields from 0.1 G, the earth's field, to up 10 kG. Thus, the initial static magnetic field distribution, B_z, can be measured and compared to the field components B_r and B_θ produced by the MRI. The probe can be mounted either radially or axially depending upon the mode information desired.

ing conducting fluid. We expect that the radial perturbations from the MRI and their azimuthally sheared result will produce a fluctuating B_r and B_θ field from an original imposed static B_z field through MRI growth. These fluctuating fields are the result of the linear and nonlinear growth of the various MRI modes transformed by the difference of the sheared Couette flow at a given radius and the probe angular velocity, Ω_2, of the outer cylinder. A significant difficulty will be the observation of the linear growth of any particular MRI mode because the time constant for establishing the initial axial field within the conducting liquid sodium will be long, $\sim 30/\Omega_2$, compared to the expected growth rate, $\sim\Omega_2$, of the instabilities as derived in this paper. We therefore expect to observe primarily the near steady state of the nonlinear limit of various modes, but the sequential linear phases may be observed during the comparatively slow rise of the field. If the applied field or flux is amplified by the MRI, such as a dynamo, then we expect to see fluctuating fields significantly greater than the applied field. In addition since the inner and outer cylinders are driven separately, the relative torque as a function of the applied magnetic field becomes an integral diagnostic of the nonlinear limits of the instability growth.

By driving the inner cylinder and applying a variable brake with a corresponding torque measurement to the outer cylinder, one can explore the full range of Couette velocity profiles, including the marginal Couette flow hydrodynamic stability condition discussed next. This condition of maximum or marginal stable Couette profile can be established in the experiment precisely by gear ratios, and so the degree of turbulence measured by the torque can be explored at the stability boundary. In addition, the pressure will be measured at five radii and compared to the pressure distributions expected of the various Couette profiles. A finite torque measurement can be interpreted in terms of turbulence existing between the two cylinders. No turbulence or perfectly laminar flow will exert a torque on the order of $1/\mathrm{Re}$, Re the fluid Reynolds number where $\mathrm{Re} \simeq 10^7$, compared to a turbulent torque, $\sim 1/\mathrm{Re}^{1/2}$, if the Ekman layer circulation leads to the weak turbulence that we discuss later. This same possible weak turbulence can also be measured by introducing a very weak field, $B_{\min} \simeq 1$ G, small enough so as not to cause the growth of MRI in resistive liquid but large enough so that an unstable flow or weakly turbulent flow can be measured as fluctuations in B_r and B_θ with the Hall effect probes. Therefore, the fluid flow conditions can be fully explored before the application of magnetic fields designed to create the MRI. When the MRI does take place, then the instability can be recognized as a departure from the previously measured initial fluid state.

It is critical to have large shear rates in order to observe the maximum growth rates of the MRI. However, excessive shear will hydrodynamically destabilize the flow by the

TABLE 1
ACTUAL AND NORMALIZED QUANTITIES IN THE SODIUM AND GALLIUM EXPERIMENTS

PROPERTY	ACTUAL		NORMALIZED	
	Sodium	Gallium	Sodium	Gallium
Kinematic viscosity ν ($cm^2\ s^{-1}$)	7.1×10^{-3}	3.2×10^{-3}	3.6×10^{-8}	2.2×10^{-7}
Reynolds number Re	...	...	1.3×10^{7}	3.0×10^{6}
Magnetic diffusivity η ($cm^2\ s^{-1}$)	810	2000	4.2×10^{-3}	1.4×10^{-1}
Magnetic Reynolds number Rm	...	...	120	4.7
Density ρ ($g\ cm^{-3}$)	0.92	6.0	...	...
Alfvén speed V_A ($cm\ s^{-1}$) (10^3 G)	2.9×10^{2}	1.1×10^{2}	4.6×10^{-2}	1.2×10^{-1}
Inner radius R_1 (cm)	15.25	5	.5	.33
Outer radius R_2 (cm)	30.5	15	1	1
Length L (cm)	30.5	10.	1	0.66
Inner angular velocity Ω_1 (s^{-1})	829	533	4	8.2
Outer angular velocity Ω_2 (s^{-1})	207	65	1	1
Prandtl number Pm = Rm/Re	...	...	9.2×10^{-6}	1.6×10^{-6}
Ekman turbulent Prandtl number Pm_t	...	...	0.012	6.3×10^{-3}

Kelvin-Helmholtz instability. Let us consider a Couette flow profile in cylindrical coordinates. Take r, θ, z as the radial, azimuthal, and axial directions, respectively. The radial distribution of angular velocity of the flow, $\Omega(r)$, is given by (Landau & Lifshitz 1959)

$$\Omega(r) = \frac{\Omega_2 R_2^2 - \Omega_1 R_1^2}{R_2^2 - R_1^2} + \frac{1}{r^2}\frac{(\Omega_1 - \Omega_2) R_1^2 R_2^2}{R_2^2 - R_1^2} , \qquad (1)$$

where $R_1(R_2)$ and $\Omega_1(\Omega_2)$ are the inner (outer) radii and angular velocities.

In the limit of infinitely large hydrodynamic Reynolds number, Re, the stability condition for Couette flow, is given by $\Omega_1 R_1^2 < \Omega_2 R_2^2$ (Landau & Lifshitz 1959). Therefore, in order to maximize the shear flow within the apparatus, the NMD experiment has been designed such that $R_2/R_1 = 2$ and $\Omega_1/\Omega_2 = 4$, guaranteeing that $\Omega_1 R_1^2 = \Omega_2 R_2^2$. In addition to stability constraints, stress limitations in the experiment require that an upper limit of $\Omega_2 = 33$ Hz be placed on the frequency of rotation of the outer cylinder. Of course, the lower rotation rate can be used in both the NMD and PPPL experiments, but it is assumed for this analysis that the highest rates are of greatest scientific interest.

The assumption of stable Couette flow implies a laminar flow with no turbulence. On the other hand, the initial acceleration of the fluid to the final state of Couette flow from an alternate initial state implies a transient enhanced torque because, just as in the accretion disk, the laminar friction is too small. However, in the experimental apparatus, the transient Couette flow profile is Helmholtz unstable so that turbulence is a natural and expected result of the "spin-up" of the flow.

On the other hand, the Ekman flow creates a relative torque between Ω_1 and Ω_2 that we expect to be balanced by a weak turbulence as observed by Taylor (1936) and analogous to the spin-up turbulence. This turbulence may also influence the stability conditions, but primarily influences the ability to distinguish turbulence caused by the MRI from the hydrodynamic turbulence caused by the Ekman layer. We therefore analyze the MRI stability conditions as a function of hydrodynamic turbulence preexisting in the liquid and therefore of the Prandtl number. At large enough levels of turbulence, the effective electrical resistivity can also be increased and therefore decrease the magnetic Reynolds number, Rm, and therefore influence the conditions of excitation of the MRI.

In comparison to the New Mexico dynamo experiment, a similar experiment at the Princeton Plasma Physics Laboratory has been proposed to look for the MRI in a rotating liquid metal annulus (Ji et al. 2001). The PPPL experiment utilizes liquid gallium, an easy to handle metal with properties similar to liquid sodium (see Table 1). Note, however, the higher density and higher resistivity of liquid gallium, which limit the maximum rotation speed and the maximum achievable Rm. The dimensions of the PPPL experiment are slightly different, enabling them to acquire larger shear flow rates (Ji et al. 2001). For $R_1 = 5$ cm and $R_2 = 15$ cm, then $R_2/R_1 = 3$ with a typical $\Omega_1/\Omega_2 = 9$. The conditions for instability for both experiments are discussed in § 4.

3. LOCAL STABILITY ANALYSIS

The angular velocity of Couette flow confined between coaxial cylinders with radii $R_1 < r < R_2$ and cylindrical angular velocities Ω_1, Ω_2 is given by

$$\Omega(r) = a + \frac{b}{r^2} , \qquad (2)$$

where we define a and b as

$$a = \frac{\Omega_2 R_2^2 - \Omega_1 R_1^2}{R_2^2 - R_1^2} ,$$
$$b = \frac{(\Omega_1 - \Omega_2) R_1^2 R_2^2}{R_2^2 - R_1^2} . \qquad (3)$$

The incompressible and dissipative MHD equations describing the dynamics of liquid metals are given as

$$\nabla \cdot \boldsymbol{B} = 0 , \qquad (4a)$$
$$\nabla \cdot \boldsymbol{V} = 0 , \qquad (4b)$$
$$\frac{\partial \boldsymbol{B}}{\partial t} = \nabla \times (\boldsymbol{V} \times \boldsymbol{B}) + \eta \nabla^2 \boldsymbol{B} , \qquad (4c)$$
$$\frac{\partial \boldsymbol{V}}{\partial t} + (\boldsymbol{V} \cdot \nabla)\boldsymbol{V} = \frac{(\boldsymbol{B} \cdot \nabla)\boldsymbol{B}}{4\pi\rho} - \frac{1}{\rho}\nabla\left(p + \frac{B^2}{8\pi}\right) + \nu \nabla^2 \boldsymbol{V} , \qquad (4d)$$

where $\boldsymbol{B}$ is the magnetic field, $\boldsymbol{V}$ is the velocity, η is the magnetic diffusivity, p is the pressure, and ν is the kinematic viscosity. In cylindrical symmetry, the system of equations (4a)–(4d) have stationary solution $\boldsymbol{V}_0 = [0,\ r\Omega(r),\ 0]$ and $\boldsymbol{B}_0 = [0,\ B_{\theta 0}(r),\ B_{z0}]$, where B_{z0} is a constant, $B_{\theta 0} \propto 1/r$, and the angular velocity profile, $\Omega(r)$, is given by equation (2). One needs to investigate the time evolution of perturbations to this equilibrium state governed by the linearization of system of equations (4a)–(4d). A similar analysis of perturbations was performed by Goodman & Ji (2001), who showed that local WKB approximation gives results for growth rates of instability, which are close to the growth rates obtained by solving the full boundary value problem in radial direction. As it is especially stressed by Ji et al. (2001) and Goodman & Ji (2001), WKB local analysis leads to a good approximation of the growth rates even in the case of the scale of perturbations being equal to or comparable to the sizes of the vessel. Thus, in this work, we limit ourselves to the local approach, which is much easier to carry out than the full eigenmode analysis, because it allows one to obtain an algebraic dispersion relation. The perturbations $\boldsymbol{b} = (b_r,\ b_\theta,\ b_z)$, $\boldsymbol{v} = (v_r,\ v_\theta,\ v_z)$ are assumed to be axisymmetric and proportional to $\exp(\gamma t - ik_z z - ik_r r)$, where γ is the associated growth rate. It is also assumed that the minimum possible wavenumbers in r and z directions are $k_r = \pi/(R_2 - R_1)$ and $k_z = \pi/L$. The linearized equations of motion are then given by

$$0 = \left(\frac{1}{r} - ik_r\right) v_r - ik_z v_z \ , \tag{5a}$$

$$0 = \left(\frac{1}{r} - ik_r\right) b_r - ik_z b_z \ , \tag{5b}$$

$$\gamma b_r = -ik_z B_{z0} v_r - \eta k^2 b_r \ , \tag{5c}$$

$$\gamma b_\theta = -ik_z B_{z0} v_\theta + \frac{d\Omega}{d\ln r} b_r - r v_r \frac{d}{dr}\left(\frac{B_{\theta 0}}{r}\right) - \eta k^2 b_\theta \ , \tag{5d}$$

$$\gamma v_r - 2\Omega v_\theta = -\frac{1}{4\pi\rho}\left(ik_z B_{z0} b_r + \frac{2B_{\theta 0}}{r} b_\theta\right) + ik_r \frac{p_1}{\rho} - \nu k^2 v_r \ , \tag{5e}$$

$$\gamma v_\theta + \frac{\kappa^2}{2\Omega} v_r = -\frac{1}{4\pi\rho}\left[ik_z B_{z0} b_\theta - b_r\left(\frac{d}{dr} + \frac{1}{r}\right) B_{\theta 0}\right] - \nu k^2 v_\theta \ , \tag{5f}$$

$$\gamma v_z = -\frac{ik_z B_{z0}}{4\pi\rho} b_z + ik_z \frac{p_1}{\rho} - \nu k^2 v_z \ , \tag{5g}$$

where the epicyclic frequency κ is defined as

$$\kappa^2 = \frac{1}{r^3}\frac{d(r^4\Omega^2)}{dr} = 4\Omega^2 + \frac{d\Omega^2}{d\ln r} \ , \tag{6}$$

p_1 is the perturbation of the pressure, and $k = (k_z^2 + k_r^2)^{1/2}$ is the total wavenumber, respectively. Note that κ can be expressed through a and b in equation (3) as

$$\kappa^2 = 4a\left(a + \frac{b}{r^2}\right) \ , \tag{7}$$

which vanishes when velocity shear is maximum ($a = 0$, $b = r^2\Omega$).

These equations lead to the following local dispersion relation

$$\left[(\gamma + \nu k^2)(\gamma + \eta k^2) + k_z^2 V_{\rm A}^2\right]^2 \frac{k^2}{k_z^2} + \kappa^2(\gamma + \eta k^2)^2 + \frac{d\Omega^2}{d\ln r} k_z^2 V_{\rm A}^2 + \frac{2ik_z V_{{\rm A}\theta z}^2}{r}\left[(\gamma + \nu k^2)\frac{d\Omega}{d\ln r} - \frac{\kappa^2}{2\Omega}(\gamma + \eta k^2)\right] = 0 \ , \tag{8}$$

where

$$V_{{\rm A}\theta z}^2 = \frac{B_{\theta 0} B_{z0}}{4\pi\rho} \ , \quad V_{\rm A}^2 = \frac{B_{z0}^2}{4\pi\rho} \ . \tag{9}$$

Neglecting all $1/r$ terms compared to k yields the following dispersion relation, which is identical to the dispersion relation derived by Ji et al. (2001):

$$\left[(\gamma + \nu k^2)(\gamma + \eta k^2) + (k_z V_{\rm A})^2\right]^2 \frac{k^2}{k_z^2} + \kappa^2(\gamma + \eta k^2)^2 + \frac{d\Omega^2}{d\ln r}(k_z V_{\rm A})^2 = 0 \ . \tag{10}$$

In the case of maximum shear flow, $a = 0$, and hence, $\kappa = 0$, the dispersion relation simplifies to

$$\left[(\gamma + \nu k^2)(\gamma + \eta k^2) + (k_z V_{\rm A})^2\right]^2 - 4\Omega^2 \frac{k_z^4 V_{\rm A}^2}{k^2} = 0 \ , \tag{11}$$

which immediately yields the following solutions for γ

$$\gamma = \frac{1}{2}\left[-(\nu + \eta)k^2 \pm \sqrt{(\nu + \eta)^2 k^4 - 4\left(\nu\eta k^4 + k_z^2 V_{\rm A}^2 \pm \frac{2\Omega k_z^2 V_{\rm A}}{k}\right)}\right] . \tag{12}$$

Only when we take the plus sign for the square root term and the minus sign for the last term in equation (12) does it give the unstable solution, and all the other three solutions are stable.

The MRI occurs only when the second term inside the square root of equation (12) is negative; i.e.,

$$\omega_\nu \omega_\eta + \omega_{\rm A}^2 < 2\frac{k_z \Omega \omega_{\rm A}}{k} \ , \tag{13}$$

where $\omega_\nu = \nu k^2$, $\omega_\eta = \eta k^2$, and $\omega_{\rm A} = V_{\rm A} k_z$. Thus, viscosity, magnetic diffusion, and magnetic tension stabilize the MRI, whereas the shear flow destabilizes it. The condition for neglecting ν and η can be derived from equation (12) by evaluating the expression under the square root, i.e.,

$$(\nu - \eta)^2 k^4 \ll \frac{4\omega_{\rm A}(2k_z\Omega - k\omega_{\rm A})}{k} \ . \tag{14}$$

For $k_r = 0$, equation (14) further reduces to

$$\frac{(\eta - \nu)^2 k_z^2}{V_{\rm A}^2} \ll \frac{4(2\Omega - \omega_{\rm A})}{\omega_{\rm A}} \ . \tag{15}$$

Thus, it is apparent that magnetic diffusivity and kinematic viscosity only affect high k_z modes.

If the magnetic diffusivity is large and the applied magnetic field is weak, equation (12) reduces to two roots $\gamma = -\nu k^2$ and $\gamma = -\eta k^2$. The former root corresponds to a hydrodynamic branch in which the fluid is disconnected from the electromagnetic force and behaves as a pure fluid. The latter root is an electromagnetic branch, in which the magnetic field diffuses as in vacuum. With an increasing magnetic field, bifurcations occur in which the hydrodynamic and electromagnetic branches are split into four branches. When $\omega_\nu \sim \omega_A \ll \omega_\eta$, the unstable solution of equation (11) is given by

$$\gamma = -\omega_\nu + \frac{\omega_A(2\Omega - \omega_A)}{\omega_\eta - \omega_\nu} , \tag{16}$$

showing that the unstable solution emerges from the hydrodynamic branch. Although magnetic diffusion diminishes the MRI, the branch remains unstable if the condition $\omega_A > \omega_\eta\omega_\nu k/(2k_z\Omega)$ is satisfied. Note, however, that even if the magnetic diffusivity is high, a weak magnetic field is capable of generating the MRI.

Next, let us consider the hydrodynamic limit ($V_A = 0$), with arbitrary Couette flow profiles ($a \neq 0$). In this case, $\kappa \neq 0$ in general, and we have to go back to equation (10) for deriving solutions. Two trivial solutions are $\gamma = -\eta k^2$, corresponding to the electromagnetic branch, and the second is given by

$$\gamma = -\nu k^2 \pm i\kappa \frac{k_z}{k} , \tag{17}$$

which is the hydrodynamic branch.

The effect of finite κ and high ν is shown in Figure 2, where the rotation speed of the cylinders, viscosity, and magnetic diffusivity of Figure 2*a* corresponds to point C of Ji et al. (2001), and the wavenumber is fixed at $(k_z,\ r_r) = (1,\ 1)$ for Figures 2*a* and 2*c* and $(4,\ 1)$ for Figures 2*b* and 2*d*, respectively. The growth rates of the four roots of equation (10) are shown as a function of the axial magnetic field strength B_z. The epicyclic frequency κ is finite in Figures 2*a* and 2*c*, whereas $\kappa = 0$ in Figures 2*b* and 2*d*. The kinematic viscosity ν is taken as the actual value of

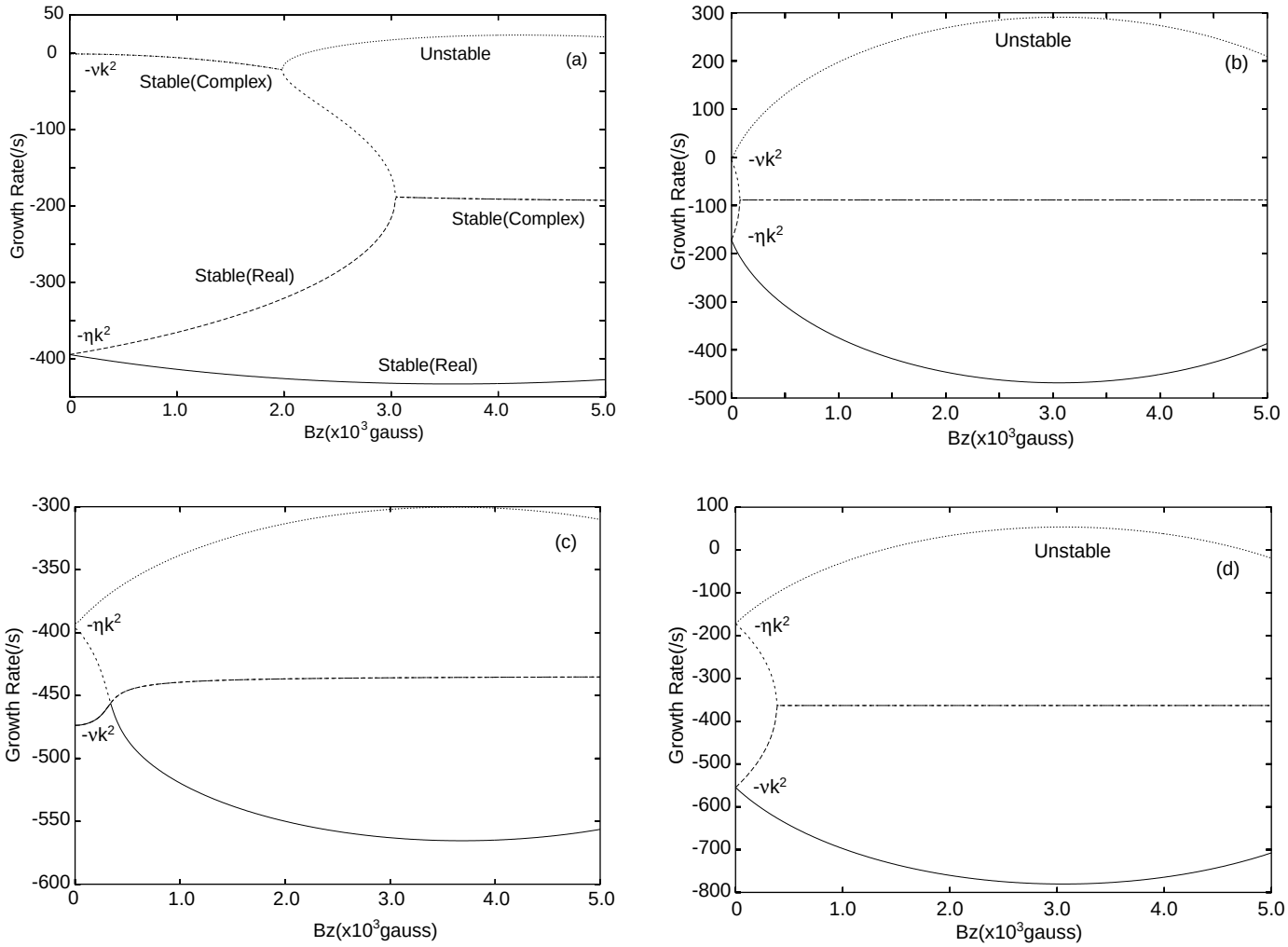


FIG. 2.—Complex stability plane of the combinations of limiting Couette and nonlimiting Couette flow profiles with laminar and turbulent flows. Panels *a* and *c* are for a nonlimiting Couette flow profile (the gallium experiment), and panels *b* and *d* are for the limiting Couette flow profile (the sodium experiments). For panels *a* and *b*, the flow is assumed as laminar ($\nu \ll \eta$); for panels *c* and *d*, the flow is turbulent ($\nu > \eta$). The corresponding Prandtl numbers are (*c*) $\mathrm{Pm}_t = 1.20$ and (*d*) 3.23. A remarkable difference between (*a*) the nonlimiting Couette and (*b*) limiting Couette profiles is the hydrodynamic branch, where $(-\nu k^2)$ is stable with the nonlimiting Couette profile and weak magnetic field, whereas it becomes unstable with a weak magnetic field and the limiting Couette flow profile. With strong turbulence (*c*, *d*), the nonlimiting Couette flow profile is always stable (panel *c*), whereas the limiting Couette flow profile becomes unstable with a strong magnetic field ($B_z > 2 \times 10^3$ G). For panels *a* and *c*, $(k_z,\ k_r) = (1,\ 1)$; for panels *b* and *d*, $(k_z,\ k_r) = (4,\ 1)$.

gallium (Fig. 2*a*) and sodium (Fig. 2*b*), whereas we make it artificially high ($\nu > \eta$) in Figures 2*c* and 2*d* to see the effect of anomalous increase of ν due to possible turbulence.

In the hydrodynamic limit ($B_z = 0$) in Figure 2*a*, the solutions of the hydrodynamic branch ($\gamma \sim 0$) are complex (eq. [17]). Near $B_z = 2000$ G, these solutions are separated, and both become real. Only one solution becomes unstable. Thus, if the flow is not a maximum shear flow profile ($\kappa \neq 0$), the MRI is stabilized for weak magnetic fields.

Figures 2*c* and 2*d* show that the turbulence suppresses the unstable MRI mode. Since the Ekman layer may make the fluid weakly turbulent, it is important to estimate the scale of this turbulence, which will be discussed in § 5.

In the next section, stability diagrams are presented and compared for both experiments.

4. STABILITY DIAGRAMS AND GROWTH RATES IN SODIUM AND GALLIUM EXPERIMENTS

The comparison between the NMD and Princeton experiments is done by comparing their typical parameters in Table 1. In order to evaluate the physical differences between the experiments, we compare the dimensionless parameters, presented in the second column of Table 1. We use R_2 and Ω_2^{-1} as units of length and time to obtain the dimensionless quantities.

We choose $\Omega_1 = 84.8$ Hz and $\Omega_2 = 10.34$ Hz as the typical values for the gallium experiment, which corresponds to point C of Ji et al. (2001). The global magnetic Reynolds number becomes

$$\mathrm{Rm} = \frac{R_2\Omega_2(R_2 - R_1)}{\eta} \ . \tag{18}$$

The Rm is higher in the sodium experiment, which is designed to observe the $\alpha\omega$ dynamo (Colgate et al. 2001; Pariev 2001). All the growth rates are evaluated at the radius $r = \bar{r}$, which satisfies $\Omega(\bar{r}) = (\Omega_1\Omega_2)^{1/2}$. We also define the global fluid Reynolds number as

$$\mathrm{Re} = \frac{R_2\Omega_2(R_2 - R_1)}{\nu} \ . \tag{19}$$

Using these parameters, the growth rate is obtained by solving equation (10) numerically, and the unstable regions are plotted in Figure 3 as a function of axial magnetic field strength and wavenumber k_z. The unit of k_z is $\pi/(R_2 - R_1)$, k_r is π/L in Figures 3–6 and 8–10. The minimum possible values for the dimensionless k_r and k_z are unity. We fixed k_r as unity in Figure 3. Notice that in both experiments, a strong field suppresses high k modes because of the magnetic diffusivity and magnetic tension. In the sodium case (Fig. 3*a*), higher k_z modes are destabilized, and the growth rate is higher compared to the gallium case (Fig. 3*b*). In the gallium case, the suppression of the unstable modes with low magnetic field occurs because of finite κ (see § 3 for details).

Figures 4 and 5 demonstrate the dependence of the growth rate on the wavenumbers in the sodium and gallium experiments. In Figure 4, an axial magnetic field B_z is fixed at 3×10^3 G, and in Figure 5 at 400 G. When $B_z = 3 \times 10^3$ G, a number of k_z modes ($k_z < 8$) are destabilized in the sodium experiment (Fig. 4*a*), while in the gallium experiment (Fig. 4*b*), only the $k_z = 1$ mode is destabilized.

A more significant difference between the sodium and gallium experiments is shown in Figure 5. For weak magnetic fields, no mode is unstable in the gallium experiment (Fig. 5*b*), whereas higher k_z modes ($k_z > 50$) are excited in the sodium experiment (Fig. 5*a*). As we noted before, the finite κ suppresses the unstable MRI modes with weak magnetic field.

In order to show the importance of the maximum shear, we plot the growth rate for the gallium experiment with $\kappa = 0$ in Figure 6. We reproduce Figures 3*b*, 4*b*, and 5*b* in Figures 6*a*, 6*b*, and 6*c*, respectively, except we take $\Omega_2 = \Omega_1/9$ for the maximum shear (see eqs. [3] and [7]). In Figure 6*a*, high k_z modes are unstable with low magnetic

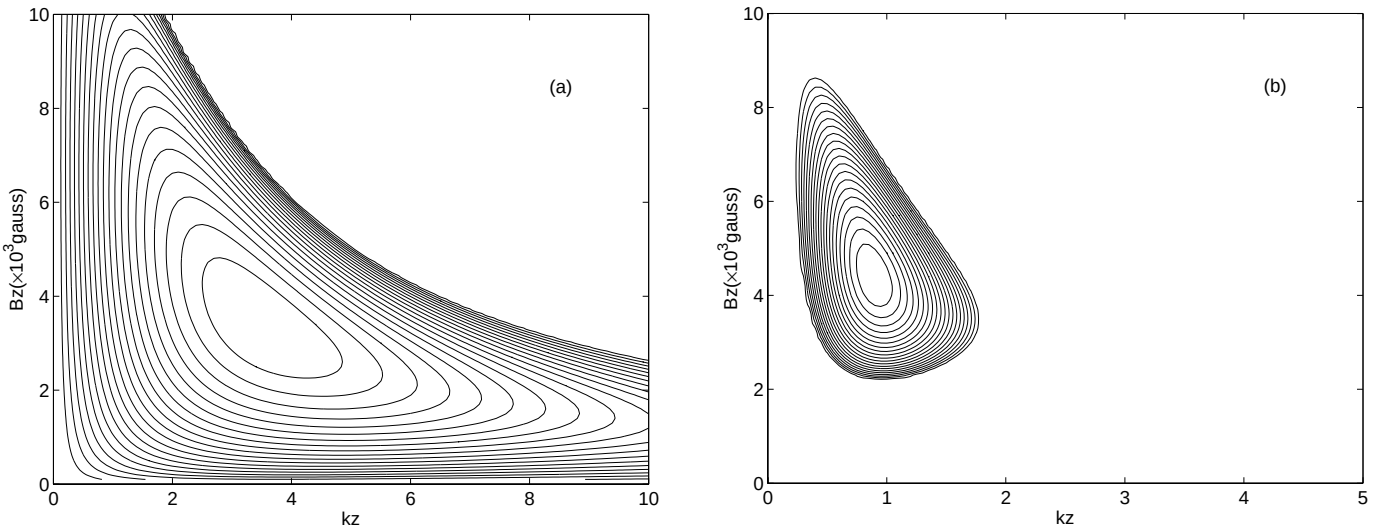


FIG. 3.—Growth rates of the MRI in (*a*) sodium and (*b*) gallium experiments. Growth rates are shown as a function of k_z and B_z. All the contours of contour figures are equally spaced, and only positive growth rate contours are shown. The radial wavenumber k_r is fixed to be unity for both calculations. When $B_z = 3 \times 10^3$ G, $k_z = 4$ mode is the most unstable mode with $\gamma = 300$ s^{-1} for (*a*) the sodium experiment, whereas $k_z = 1$ with $\gamma = 25$ s^{-1} for (*b*) the gallium. Higher k_z modes are destabilized with weak magnetic field in the sodium experiment, but with strong magnetic field, they are suppressed by the magnetic diffusivity and magnetic tension. Weak magnetic field modes in gallium are suppressed because of finite κ (see Fig. 6).

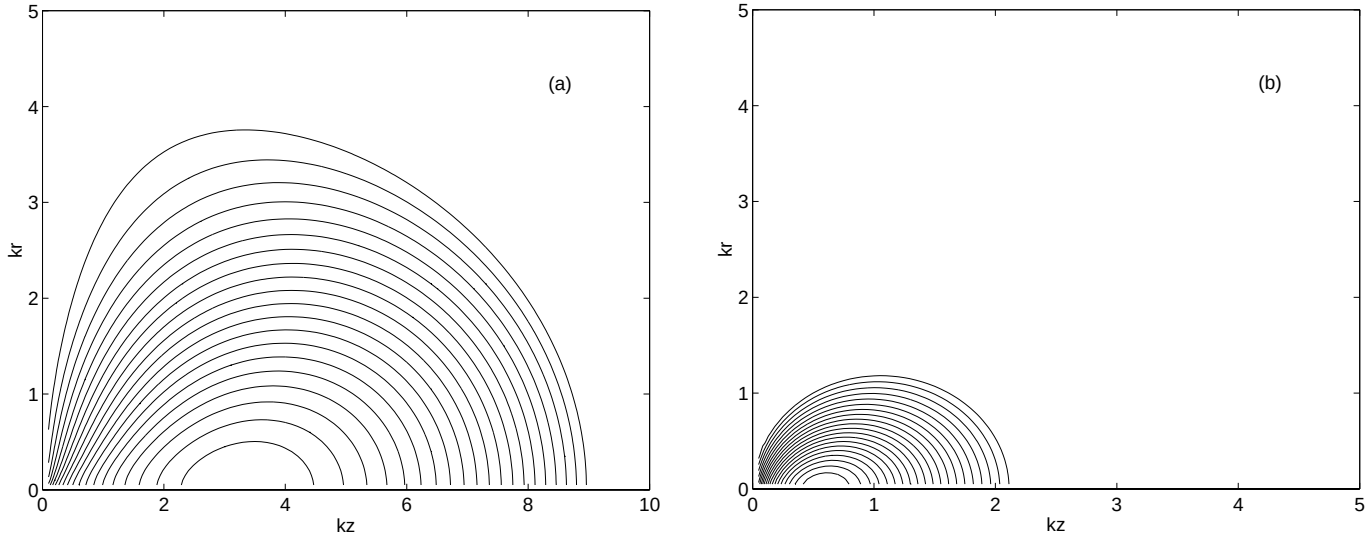


FIG. 4.—Growth rates as a function of wavenumbers. An axial magnetic field strength is fixed at 3000 G for both experiments. The value of the maximum contour is (*a*) 350 s^{-1} and (*b*) 100 s^{-1}. The growth rate decreases with k_r for both experiments. Up to $k_z = 8$ modes are unstable in (*a*) the sodium case, whereas only the $k_z = 1$ mode is unstable in (*b*) the gallium case. Other parameters are taken from Table 1.

field, which are stable with finite κ (Fig. 3*b*). Maximum velocity shear also destabilizes high k_r modes (Figs. 6*b* and 6*c*), so many modes will be excited in the gallium experiment at maximum shear. In all cases, the $(k_z, k_r) = (1, 1)$ mode is dominant, but mode coupling may occur in the nonlinear regime to excite turbulence in the gallium experiment.

While the maximum shear flow profile leads to easy excitation of MRI, it falls on the border line for pure hydrodynamic instability. We show the contour plot of the unstable region for the modes $(k_r, k_z) = (1, 2)$ and $(3, 5)$ of the sodium experiment in Figure 7. In the regime $\Omega_2/\Omega_1 < 0.25$, sodium is hydrodynamically unstable. The maximum shear flow is indicated as a solid line. High wavenumber modes are unstable only near the maximum shear flow and weak magnetic field in the hydrodynamically stable region (Fig. 7*b*). Growth rates for the finite κ shear case are shown in Figure 8. High wavenumber modes are stabilized compared to the $\kappa = 0$ case, Figure 6, but several modes are still unstable. Comparison of Figure 3*b* to Figure 8*a* and Figure 4*b* to Figure 8*b* shows that even for highly subcritical flow with $\Omega_1/\Omega_2 = 2$, the sodium experiment will allow one to observe more MRI unstable modes than the gallium experiment for slightly subcritical flow with $\Omega_1/\Omega_2 = 8.2$ (Ji et al. 2001, point C). Thus, the sodium experiment has a higher potential for the observation of turbulence due to the nonlinear development of the MRI at the rotation profiles with smaller shear, i.e., when the flow is highly stable in the absence of the magnetic fields.

5. TURBULENCE DERIVED FROM THE EKMAN LAYER FLOW

We believe we need to understand the minimum expected turbulence level in the fluid before attempting to observ-

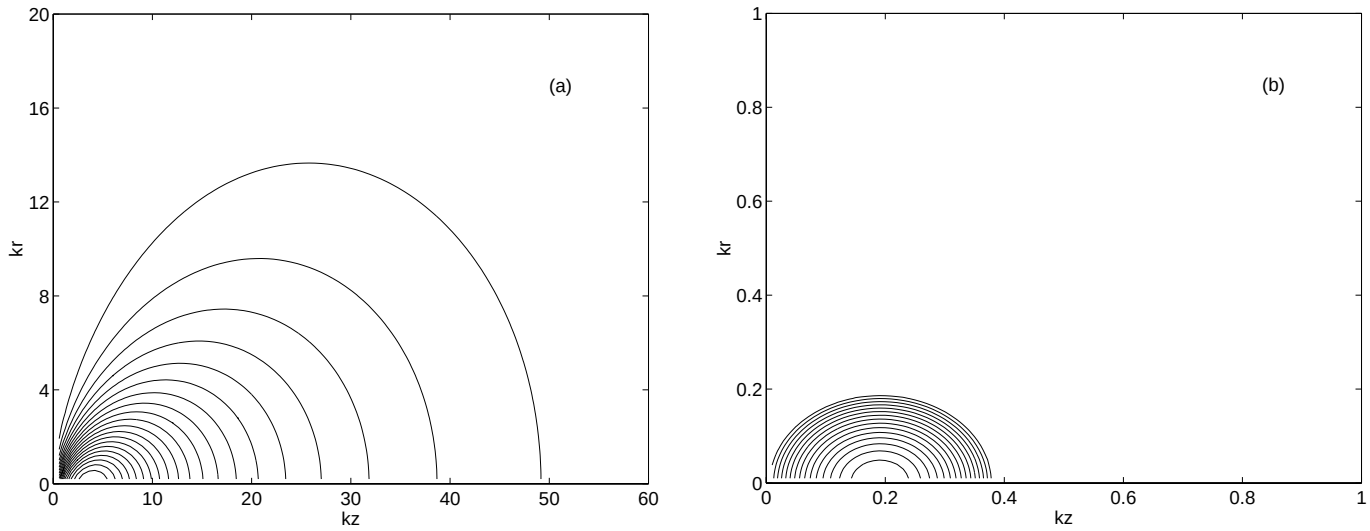


FIG. 5.—Same as Fig. 4, but with $B_z = 400$ G. The value of the maximum contour is (*a*) 130 s^{-1} and (*b*) 7.0 s^{-1}. No mode is destabilized in (*b*) the gallium case, whereas high k_z modes are excited in (*a*) the sodium case.

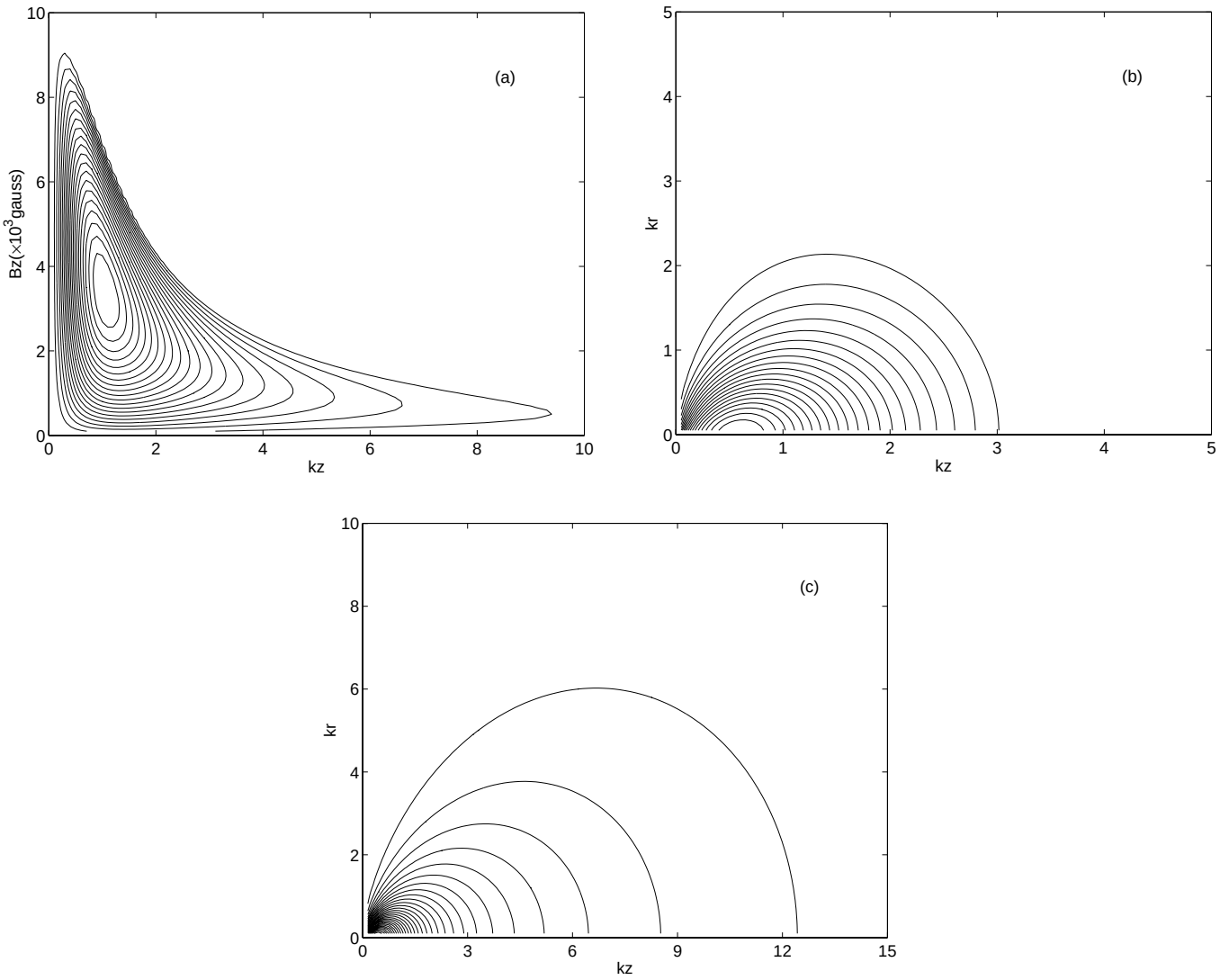


FIG. 6.—Growth rates of the MRI in the gallium experiment with $\kappa = 0$. All the parameters are the same as point C in Ji et al. (2001) except $\Omega_2 = \Omega_1/9$. The value of the maximum contour is (*a*) 35 s^{-1}, (*b*) 100 s^{-1}, and (*c*) 30 s^{-1}. (*a*) Growth rate with $k_r = 1$. When $B_z < 4.5 \times 10^3$ G, $k_z = 2$, and higher modes are destabilized because of maximum shear rate ($\kappa = 0$). (*b*) With $B_z = 3.0 \times 10^3$ G. High k_r modes, which are stable in the finite κ case (Fig. 4*b*), are unstable. (*c*) With $B_z = 4.0 \times 10^2$ G. High wavenumber modes ($k_r \leq 15,\ k_z \leq 22$) are unstable, whereas no mode is unstable in the finite κ case (Fig. 5*b*).

ationally separate the MRI growth from an unknown background. Of course that background will be measured first, but this section deals with an estimate of its magnitude. First we must point out that if there were no initial turbulence in the flow, then the expectation of laminar flow is that the torque or power required to drive the experiment would be negligibly small. Instead, since we know that there must be a torque associated with the Ekman layer flow and therefore a minimum power required to drive the Couette flow, we calculate this and compare it to the observed instability based upon the gradient of angular momentum (Richard & Zahn 1999).

Richard & Zahn (1999) have extensively reviewed the earlier experimental work on Couette flow of Wendt (1933) & Taylor (1936). In the maximally stable case where the outer cylinder rotates at Ω_2 and the inner one is stationary, $\Omega_1 = 0$, and thus where the angular momentum increases outward, the flow is observed to be weakly unstable to a finite amplitude instability despite the prediction of stability for a positive angular momentum gradient. This observed instability has been invoked by Richard & Zahn (1999) as a possible mechanism for the α-viscosity of Keplerian accretion disks. The implication is that the free energy of the flow is accessed through a finite amplitude instability producing turbulence. However, this turbulence in the positive angular momentum gradient, theoretically stable regime, is observed to be much weaker then the inverse case, exerting a much smaller torque than the turbulence generated by the unstable Couette flow, which in turn is self-excited by the flow of free energy through the turbulence itself. This lack of equivalence causes us to ascribe the occurrence of turbulence in the stable flow case to the back-reaction to the torque of the Ekman layer flow. We calculate this back reaction turbulence here as the likely lower limit of turbulence for these experiments. The initial experimental measurement of the torque, as well as the in situ magnetic fluctuations for very low fields, can and will be compared to these predictions. Finally, we note that the predicted ratio between the torques for the stable and unstable flows, based on the Ekman layer flow $G_{\rm st}/G_{\rm unst} \simeq {\rm Re}^{1/2}/{\rm Re}$, roughly

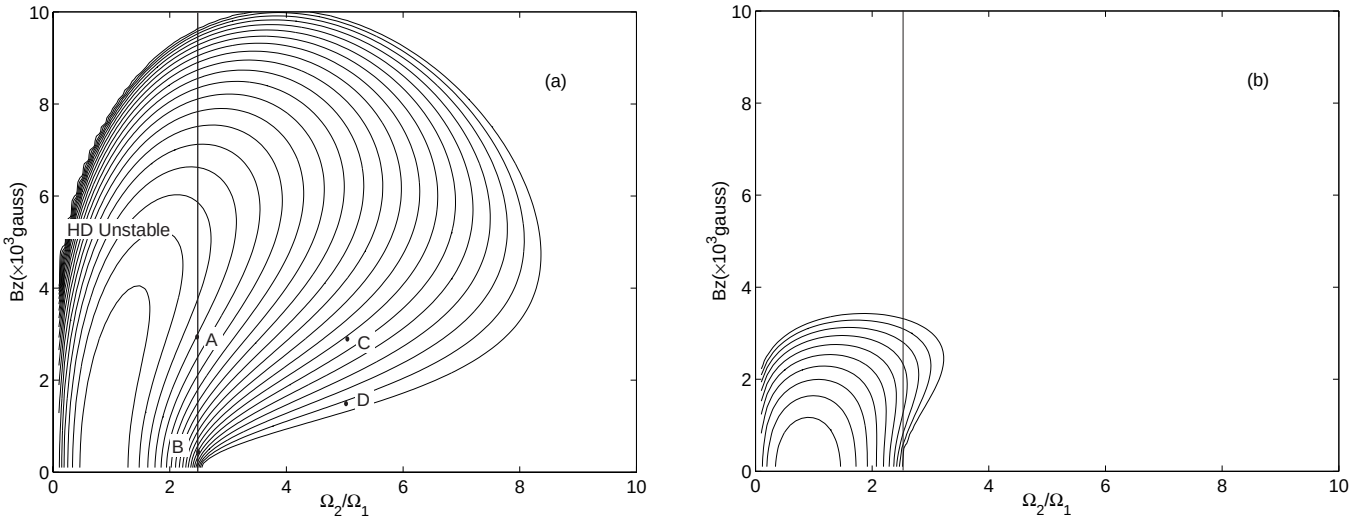


FIG. 7.—MRI unstable region of sodium experiment for two different modes. Mode number is fixed as (*a*) $(k_r,\ k_z) = (1,\ 2)$ and (*b*) $(3,\ 5)$. The value of the maximum contour is (*a*) 270 s^{-1} and (*b*) 250 s^{-1}. The region $\Omega_2/\Omega_1 < 0.25$ is hydrodynamically unstable. Parameters of point A correspond to those of Figs. 3*a* and 4*a*, point B to those of Fig. 5*a*, point C to Figs. 8*a* and 8*b*, and point D to Fig. 8*c*, respectively.

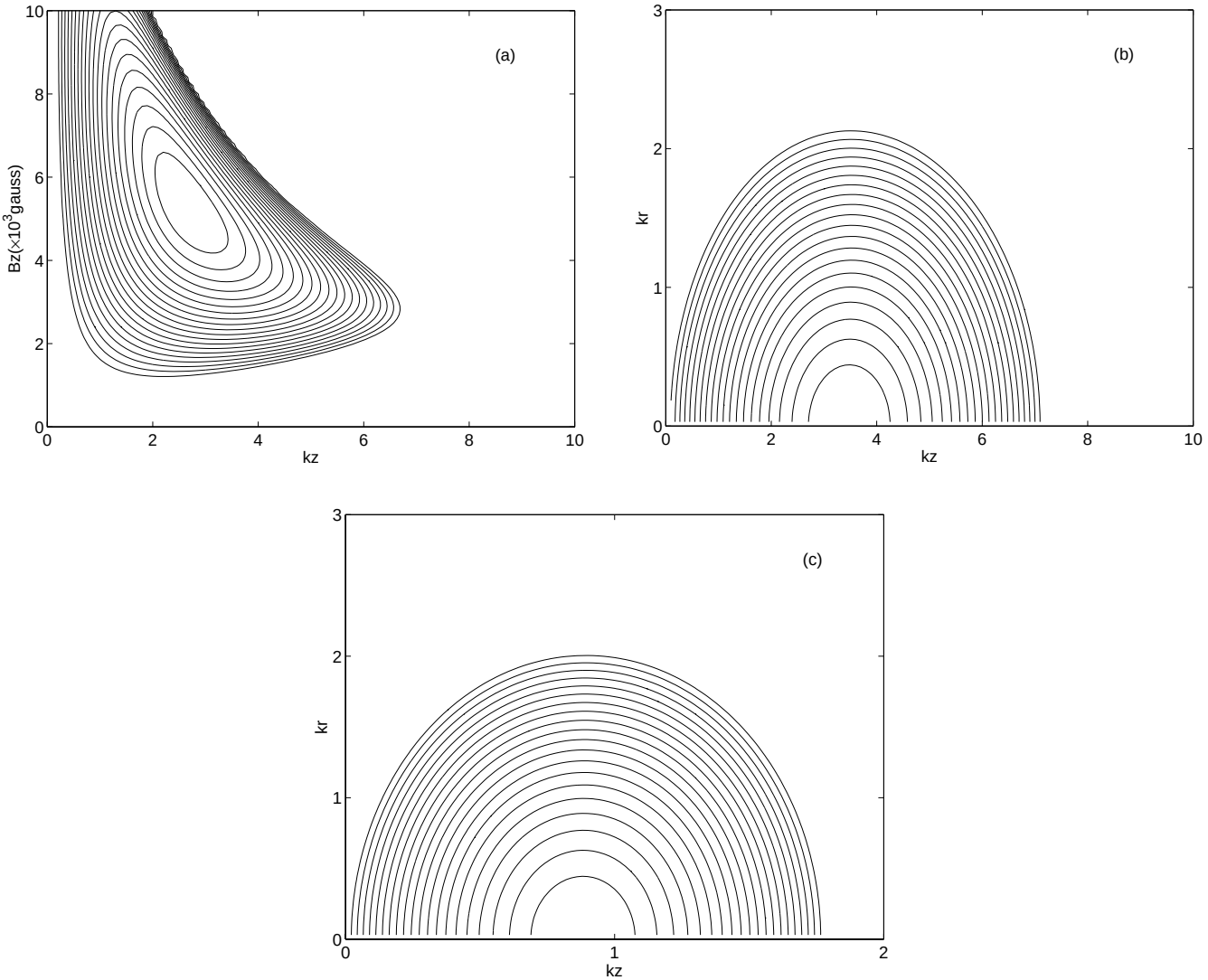


FIG. 8.—MRI growth rates with finite κ flow shear, $\Omega_2/\Omega_1 = 0.5$, for sodium experiment (Table 1). (*a*) The wavenumber k_r is fixed as unity; (*b*) with $B_z = 3 \times 10^3$ G; (*c*) with $B_z = 1.5 \times 10^3$. The value of the maximum contour is (*a*, *b*) 170 s^{-1} and (*c*) 65 s^{-1}. High wavenumber modes are suppressed in each case.

agrees with the measurements of Taylor (1936). We delay until a later paper a full analysis of this problem but give here an estimate of this expected turbulent viscosity as compared to the purely laminar one.

An Ekman layer forms adjacent to the surfaces of the end walls. This flow is both radial and azimuthal, thin, laminar, and high speed. The resulting flux of angular momentum creates a torque on the fluid and an unstable velocity profile between the inner and outer cylinders. The unstable shear flow at both the inner and outer cylindrical boundaries results in a "law of the walls" or "logarithmic profile" turbulent boundary layer (Schlichting 1960) with each of the cylinder walls. This turbulence extends from the inner to the outer differentially rotating cylinders and creates the turbulent stress necessary to transfer the torque between them.

The assumption of the stability of Couette flow in the experiment is limited by the formation of an Ekman layer adjacent to the surfaces of the end plates. Since these end plates corotate with the outer frequency Ω_2, then at any radius $r \leq R_2$ the fluid will be rotating faster than the end wall. An Ekman layer forms (Prandtl 1952) when the centrifugal force is not balanced by a pressure gradient. The pressure in the Ekman layer is the same as the pressure in the bulk of the cylinder, but the centrifugal force is smaller in the Ekman layer because of friction with the end wall. As a result, a (negative) radial flow develops in a thin layer of thickness δ with a mean radial velocity $\langle v_r \rangle \simeq r\Omega/2$ while undergoing a mean azimuthal motion $\langle v_\theta \rangle \simeq r\Omega/2$. The analysis of Prandtl (1952) results in the thickness $\delta \simeq r/(\mathrm{Re})^{1/2} = (\nu/\Omega_2)^{1/2} \simeq 5.6 \times 10^{-3}$ cm in sodium and 7.0×10^{-3} cm in gallium, using the parameters of Table 1. Hence, a radial (negative) current, F_r, flows on the order of

$$F_r \simeq -\delta(2\pi R_2)R_2\Omega_2/2 = -\pi R_2^3\Omega_2/\sqrt{\mathrm{Re}}\ \mathrm{cm}^3\ \mathrm{s}^{-1}\ . \quad (20)$$

This (negative) radial flow at both ends toward the axis must be balanced by a positive, slower radial flow throughout the central region. The Ekman flow merges with the central flow by a boundary layer at the inner cylinder surface resulting in a circulation within the Couette flow volume driven by the Ekman layers at each end. Since this flow represents a flux of angular momentum, $\rho F_r R_2^2\Omega_2/2$, from the inner radius, R_1, to the outer radius, R_2, there must be a torque, G, transmitted by the fluid corresponding to the difference in the flux of angular momentum between these two surfaces or

$$G_E = \rho F_r\left(R_2^2 - R_1^2\right)\Omega_2/2 = \rho(3\pi/8)R_2^5\Omega_2^2/\sqrt{\mathrm{Re}}\ , \quad (21)$$

where we have used the ratio $R_1/R_2 = 1/2$ for the sodium experiment. (A factor of 5.9×10^{-3} smaller is implied for the gallium experiment.) Not only does this torque between R_1 and R_2 determine the power required to drive the flow but also imposes a requirement for a weak turbulence within the so-called stable Couette flow in order to transmit this torque between R_1 and R_2. This level of turbulence becomes the minimum effective viscosity or turbulent viscosity, ν_t, of the MRI experiments. By way of comparison, in addition we calculate the torque as if the flow were completely laminar and compare the two torques.

The shear stress for turbulent or laminar flow, τ_t, τ_L, is characterized by either an effective turbulent viscosity, ν_t or laminar, ν_L. In the turbulent case the angular momentum flux from the Ekman layer must be balanced by the viscous stress from the rate of shearing, $A = rd\Omega/dr = -2\Omega_2 R_2^2 r^{-2}$ (see Pringle 1981) resulting in a viscous drag per unit area, $\tau_t = \rho\nu_t A = -2\nu_t\Omega_2 R_2^2 r^{-2}\rho$ and therefore a torque per unit length, $t_t = -2\pi r^2\tau_t = -4\pi\nu_t\Omega_2 R_2^2\rho$. This has the proper scaling since the torque must be independent of radius. The corresponding laminar torque per unit length, $t_L = -2\pi r^2\tau_L = -4\pi\nu_L\Omega_2 R_2^2\rho$, where the viscosity, ν_L, is fixed by the fluid properties and not variable with the strength of the turbulence. Then the total laminar torque per half length becomes $G_L = t_L L/2 = 2\pi\nu_L\Omega_2 L R_2^2\rho = 2\pi L R_2^4\Omega_2^2/\mathrm{Re}$. The ratio of the two torques becomes $G_L/G_E = (16/3)(L/R_2)\mathrm{Re}^{-1/2}$. Since Re is very large and $L/R_2 = 1$, the laminar torque is negligibly small compared to the Ekman layer torque, and therefore torque balance requires turbulence to enhance the effective viscosity. This effective turbulent viscosity is obtained by equating the Ekman angular momentum flux to the viscous shearing torque giving

$$\nu_t = (3/16)\frac{R_2}{L}\frac{R_2\Omega_2}{\sqrt{\mathrm{Re}}}R_2 = 10.0 \text{ and } 12.7\ \mathrm{cm}^2\ \mathrm{s}^{-1}\ , \quad (22)$$

for the sodium and gallium experiments, respectively.

The structure of this turbulence is problematic. It has been described by (Taylor 1936) as initially a series of long parallel vortices, "Taylor columns," that extend the full length of the annular space and that at greater Re these columns break up, becoming fully developed turbulence. We expect at some value of magnetic field strength that these vortices will be suppressed by magnetic field of sufficient strength. It seems unlikely, however, that a return to laminar flow would take place, because the flow profile, with no turbulent shear stress, but still the Ekman flow, will become more distorted from the stable profile resulting in stronger turbulent drive. However, for now, we defer analysis and expect guidance from future experiment.

Finally, a turbulent magnetic Prandtl number, Pm_t, for measuring the strength of this Ekman driven turbulence, can also be estimated as

$$\mathrm{Pm}_t = \frac{\nu_t}{\eta} = 0.012 \text{ and } 6.3 \times 10^{-3}\ , \quad (23)$$

respectively. Despite the very small size of the Ekman layer, the turbulence generated by such a flow influences the ability to distinguish turbulence caused by the MRI at low values of magnetic field from the hydrodynamic turbulence caused by the Ekman layer. At higher values of the magnetic field, above that affected by the Ekman turbulence, the effects caused by the MRI should be clearly recognizable.

Figure 9 shows the dependence of the MRI growth rate with the turbulent ν_t as a function of an axial magnetic field strength and the Prandtl number for the most unstable modes in both experiments. In sodium experiment, higher k_r modes are also unstable. Figure 10 shows the growth rate for $(k_r,\ k_z) = (3,\ 4)$ mode. Note that this mode is stable in gallium, even with laminar viscosity only. Finite κ for the gallium experiment prevents the MRI from developing with weak magnetic field (compare Figs. 3*b* and 6*a*, Figs. 4*b* and 6*b* above), and MRI exists only in the region $3 \times 10^3\ \mathrm{G} < B_z < 6 \times 10^3\ \mathrm{G}$ (Fig. 3*b*). However, the sodium experiment with maximum shear, $\kappa = 0$, can be destabilized with already very weak magnetic field, in the range of $50\ \mathrm{G} < B_z < 100\ \mathrm{G}$.

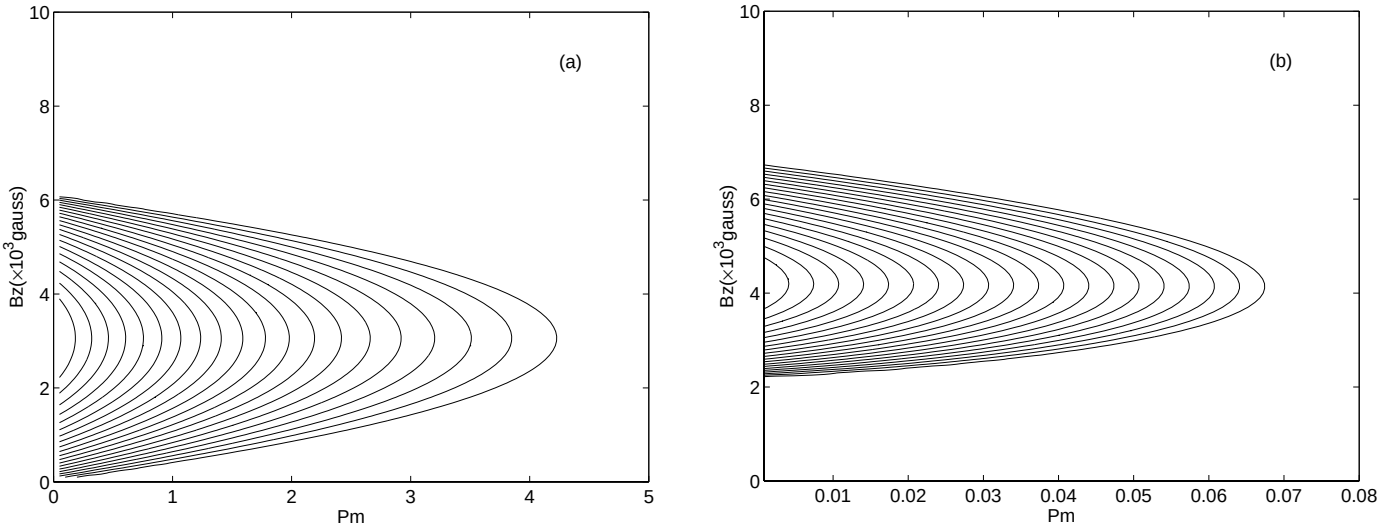


FIG. 9.—Effect of turbulence on the MRI for the (*a*) sodium and (*b*) gallium cases. The growth rate is plotted as a function of an axial magnetic field and a magnetic Prandtl number. Wavenumbers are fixed for the maximum growth rate of each experiment [$(k_r,\ k_z) = (1,\ 4)$ for sodium, $(1,\ 1)$ for gallium]. The value of the maximum contour is (*a*) 280 s^{-1} and (*b*) 23 s^{-1}. The growth rate decreases when the turbulent viscosity increases. The MRI can be sustained in fully turbulent fluid in both cases for the minimum Ekman layer driven turbulence ($Pm = 0.012$ for sodium, $Pm = 6.3 \times 10^{-3}$ for gallium).

In conclusion, the presence of Ekman layers is significant for the determining of the power necessary to sustain the differential rotation in the apparatus but has a negligible effect on the condition of the excitation of the MRI as it has been already mentioned briefly in Ji et al. (2001). However, the turbulence excited due to the presence of Ekman layers may interfere with our measurements of perturbations of magnetic field excited by the MRI. Therefore, the presence of weak turbulent perturbations due to Ekman layers seems unavoidable whenever one observes the excitation of the MRI. It also seems unlikely that the imposed magnetic field in both sodium and gallium experiments can significantly exceed a value of a few thousand gauss. The characteristic amplitude of the perturbations of the magnetic field due to the Ekman layer turbulence is $\sim B_z \lambda v_t/\eta \approx \mathrm{Pm}_t B_z$. The typical value of such perturbed magnetic fields is on the order of 1% of the applied field (see Table 1 for Pm_t), thus, limiting the possible MRI measurements of growing fields to more than 1% of the initial magnetic field.

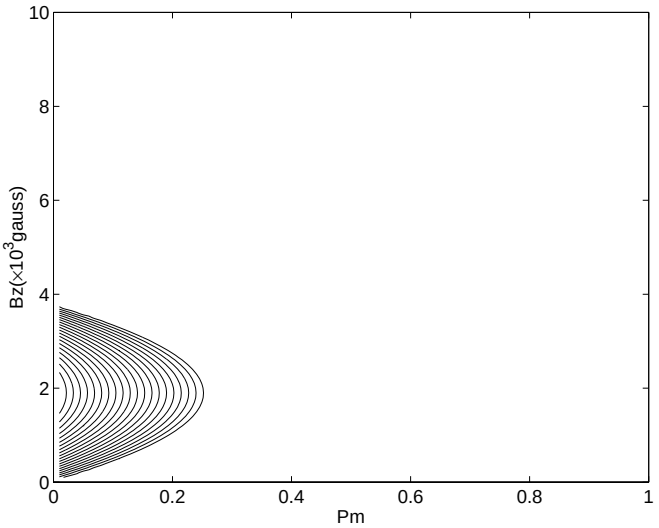


FIG. 10.—Effect of the turbulence on the MRI for the mode $(k_r,\ k_z) = (3,\ 4)$ in the sodium experiment. The value of the maximum contour is 90 s^{-1}. Note that this mode is stable in gallium even without turbulence. This mode will remain unstable even with turbulence. The critical Prandtl number for this mode to become stable is $Pm \simeq 0.3$.

6. DISCUSSION AND CONCLUSIONS

There are several aspects of each experiment that warrant discussion. The first deals with the analysis performed for both experiments. In this paper we used the full dispersion relation, which depended not only on an azimuthal magnetic field but also has all terms proportional to $1/r$ retained. This corresponds to the geometrical effect of the curvature from the cylindrical geometry. Only when one neglects all $1/r$ terms in the dispersion relation does one obtain the results of Ji et al. (2001). This allows us to consider many different magnetic field configurations, some of which will be suitable for studying the MRI.

Nevertheless, even with these significant problems and differences, it should be noted that both the NMD and PPPL experiments have an excellent chance of observing the MRI in the laboratory. Both experiments obtain very high growth rates under varying conditions yielding a flexible set of opportunities.

Finally, we note that the effect of an azimuthal magnetic field and an analysis of nonaxisymmetric modes are still open problems. Noguchi et al. (2000) showed that the local dispersion analysis in shear flow may fail even for the qualitative estimation of growth rates. The eigenmode analysis for nonaxisymmetric modes is necessary for further understanding of the MRI instability in the NMD experiment. We are now developing the shooting method code for solving equations (4a)–(4d) simultaneously. Spatial dependence of the radial wavenumber and azimuthal magnetic field dependence will be analyzed.

K. N. and S. A. C. are particularly indebted to Hui Li of Los Alamos National Laboratory for pointing out the

relevance of the MRI to the NMD experiment and encouraging the present work. V. P. thanks Eric Blackman for stimulating conversations and acknowledges partial support from DOE grant DE-FG02-00ER54600. We all acknowledge important comments by the referee, which significantly improved the article. In addition, this work has been supported by the DOE, under contract W-7405-ENG-36.

REFERENCES

Balbus, S. A., & Hawley, J. F. 1991, ApJ, 376, 214
Chandrasekhar, S. 1960, Proc. Natl. Acad. Sci., 46, 253
Colgate, S. A., Pariev, V. I., Beckley, H. F., Ferrel, R., Romero, V. D., & Weatherall, J. C. 2001, preprint (astro-ph/0112541)
Gammie, C. F. 1996, ApJ, 457, 355
Goodman, J., & Ji, H. 2001, preprint (astro-ph/0104206)
Hawley, J. F., & Balbus, S. A. 1991, ApJ, 376, 223
Hawley, J. F., Gammie, C. F., & Balbus, S. A. 1996, ApJ, 464, 690
Ji, H., Goodman, J., & Kageyama, A. 2001, MNRAS, 325, L1
Landau, L. D., & Lifshitz, E. M. 1959, Fluid Mechanics (London: Pergamon)
Matsumoto, R., & Tajima, T. 1995, ApJ, 445, 767
Noguchi, K., Tajima, T., & Matsumoto, R. 2000, ApJ, 541, 802
Pariev, V. I. 2001, Ph.D. thesis, Univ. Arizona
Prandtl, L. 1952, Essentials of Fluid Dynamics (New York: Hafner)
Pringle, J. E. 1981, ARA&A, 19, 137
Richard, D., & Zahn, J.-P. 1999, A&A, 347, 734
Sano, T., & Inutsuka, S. 2001, ApJ, 561, L179
Sano, T., & Miyama, S. 1999, ApJ, 515, 776
Schlichting, H. 1960, Boundary-Layer Theory (New York: McGraw-Hill)
Stone, J. M., Hawley, J. F., Gammie, C. F., & Balbus, S. A. 1996, ApJ, 463, 656
Taylor, G. I. 1936, Proc. R. Soc. London A, 157, 546
Velikhov, E. P. 1959, Soviet Phys.—JETP Lett., 36, 995
Wendt, F. 1933, Ingenieur-Archiv., 4, 577